Observation of Cartesian light propagation through a three-dimensional cavity superlattice in a silicon photonic band gap crystal

Manashee Adhikary,* Marek Kozoň, Ravitej Uppu,† and Willem L. Vos‡
Complex Photonic Systems (COPS), MESA+ Institute for Nanotechnology, University of Twente, P. O. Box 217, 7500 AE Enschede, The Netherlands

(Received 11 April 2023; accepted 11 September 2024; published 4 December 2024)

We experimentally investigate peculiar light propagation inside a three-dimensional (3D) superlattice of resonant cavities that are confined within a 3D photonic band gap. To this end, we fabricated 3D diamondlike photonic crystals from silicon with a broad 3D band gap in the near-infrared and doped them with a periodic array of point defects. In position-resolved reflectivity and scattering microscopy, we observe narrow spectral features that match well with superlattice bands in band structures computed with the plane-wave expansion. The cavities are coupled in all three dimensions when they are closely spaced ($a_{\mathrm{SL}} \leqslant 3a$), and uncoupled when they are further apart. The superlattice bands correspond to light that hops in high-symmetry directions in 3D ("Cartesian light") that opens applications in 3D photonic networks, 3D Anderson localization of light, and future 3D quantum photonic networks.

DOI: 10.1103/PhysRevResearch.6.043235

I. INTRODUCTION

Many fruitful analogies exist between waves such as light or sound that propagate through mesoscopic photonic or phononic metamaterials and the well-known propagation of elementary excitations in atomic crystals such as phonons, electron and spin waves [1–6]. The physics of both classes of waves is governed by multiple scattering from mesoscopic potentials and concomitant interferences. A peculiar class of wave transport is discretized transport with hopping in all three dimensions on superlattices, that has been demonstrated in phonons, electron and spin waves [7], but not for electromagnetic waves and light. A superlattice is a periodic arrangement of a supercell that consists itself of multiple unit cells of an underlying crystal structure [8,9]; its applications include photovoltaics since the absorption is enhanced by intermediate electron bands [10–14].

In one dimension (1D), discretized transport of light is known to occur in coupled resonator optical waveguides, where an optical resonator is so close to its neighbors that light hops from one resonator to a neighbor due to evanescent coupling [15–20]. A well-known feature is that the bandwidth of the resulting defect band is *proportional* to the hopping rate, as is known from atomic solid-state physics [21]. In a recent theoretical study, our team identified a new kind of 3D light transport in 3D superlattices called "Cartesian light" [22]. Here light waves propagate by hopping between neighboring cavities along high-symmetry Cartesian directions in space, see Fig. 1. The hopping transport leads to the appearance of defect bands in the 3D photonic band gap, as identified by both scaling and machine learning analyses [23,24]. It turns out that the bandwidths of the 3D defect bands are determined by intricate interference between hopping in many different high-symmetry directions, which does not exist in 1D [25]. This new mode of propagation opens avenues to applications in 3D classical and quantum photonic networks [26–29], 3D Anderson localization of light [30], and 3D cavity quantum electrodynamics (QED) on a distributed network. Notably, 3D cavity superlattices in a band gap reveal exciting enhancements of the local density of states (LDOS) that are central in cavity QED [31]; the novelty of 3D band gap cavity superlattices is that the enhanced LDOS is distributed over many crystalline sites, as opposed to current cQED where one typically has one localized cavity; as a result, we foresee novel distributed cQED networks.

In this paper, we perform an original experimental study of a 3D cavity superlattice, with a band of photonic states confined by a complete 3D photonic band gap. We have developed a 3D nanophotonic platform consisting of 3D photonic crystals made from silicon with a complete photonic band gap [32–34] that are doped by judiciously placing resonating cavities in a periodic fashion [22,23], see Figs. 1 and 2. Since each cavity confines light with photon energies within the band gap, photons can only propagate by effectively hopping from one cavity to a neighboring one on discrete superlattice positions in 3D. Our system differs from 1D coupled resonator arrays in 3D photonic crystals reported in Refs. [16,35] since our cavity network is 3D. We observe resonant scattering

*Present address: ASML Veldhoven, De Run 6501, 5504 DR, Veldhoven, The Netherlands Netherlands.
†Present address: Department of Physics & Astronomy, University of Iowa, Iowa City, IA 52242, USA.
‡Contact author: w.l.vos@utwente.nl

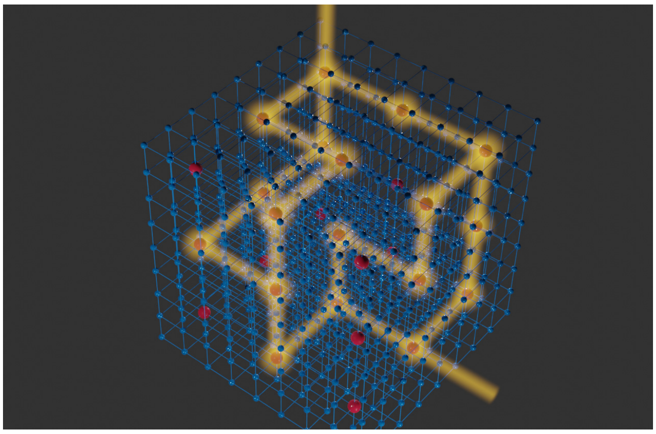

FIG. 1. Schematic of a few possible paths for waves (yellow) hopping in Cartesian directions in a finite 3D cavity superlattice. At the end of their Cartesian journey, waves may exit from a different crystal surface (top) than where they entered (right). Each cavity is shown as a red sphere and the surrounding band gap crystal as the 3D mesh with blue spheres as unit cells.

peaks that match well with theoretical defect bands. When we excite a defect on-resonance, we observe states that spatially extended over multiple superlattice positions **R**, thus corresponding to 3D coupled cavities: Cartesian light (see also Appendix A). Conversely, if we excite off-resonance, then the observed states are localized near single cavities.

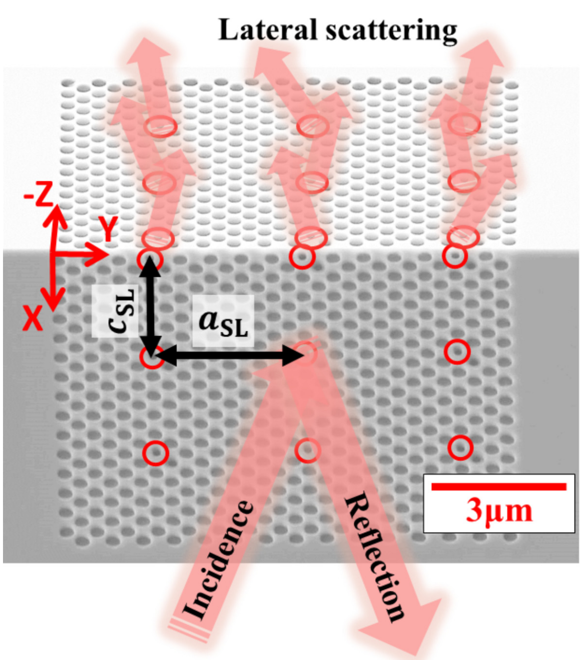

FIG. 2. Scanning electron micrograph of a 3D cavity superlattice embedded in a silicon 3D photonic band gap crystal [(X, Z) view], with lattice constants $a = 0.68$ μm (Y direction) and $c = 0.48$ μm (X and Z directions). The designed pore radius is $r = 0.16$ μm for the main nanopores and $r' = r/2 = 0.08$ μm for the defect pores. The superlattice has unit cell dimensions $5c$, $5a$, $5c$.

II. SAMPLES AND EXPERIMENTAL SETUP

The 3D photonic band gap crystals that we study have a diamondlike inverse woodpile structure [36] that consist of two arrays of nanopores with radius r running in the perpendicular X and Z directions in the high-index silicon backbone, as illustrated on YouTube [37] (see also Appendix B). Each array is centered rectangular with lattice constants $a = 680$ nm and $c = 480$ nm. By taking a ratio $a/c = \sqrt{2}$, the 3D photonic crystal has a diamondlike cubic crystal structure [36]. We employ deep reactive ion etching of silicon through a 3D etch mask on the edge of a long beam [38–40]. Silicon inverse woodpile crystals have a broad and robust 3D photonic band gap [41–44] that is well suited to confine embedded cavities and shield them from the surrounding vacuum. To define a 3D cavity in an inverse woodpile structure, we design two perpendicular and proximal defect nanopores to have smaller radii r' (see Appendix B) [45]. Near the intersection of two defect pores, the excess silicon backbone results in a donorlike cavity [34]. When multiple cavities are spaced periodically in the crystal, coupling between the cavities results in a 3D cavity superlattice that sustains Cartesian light [22].

We fabricated two types of superlattices with different spacings between the cavities, see Fig. 2 for a scanning electron microscopy (SEM) image of a real crystal. Since the defect pores are separated by five lattice constants (called SL5), the superlattice has lattice constants $a_{SL} = 5a$ in the Y and $c_{SL} = 5c$ in the X and Z directions. There are $3^2 = 9$ defect pores on each crystal surface, hence up to $3 \times 3^2 = 27$ pore crossings and concomitant cavities in the superlattice. We also studied superlattices with lattice spacings $a_{SL} = 3a$ and $c_{SL} = 3c$, called SL3, with up to $5^3 = 125$ cavities. To study the cavity superlattices, we built a confocal microscopy setup (see Appendix C, Fig. 8) that simultaneously collects both broadband specular reflectivity to probe the band gap and specular cavity scattering, and lateral scattering by the cavities into nonspecular directions, as illustrated in Fig. 1. Our setup has a near- and short-wavelength infrared (NIR and SWIR) frequency range compatible with silicon nanophotonics. The diffraction-limited focus with beam waist of 1.05 μm (at $1/e$ intensity) is less than the 3.4-μm distance between neighboring cavities in SL5. Hence, in spatial scans across the superlattice surface, we spatially probe both *on* and *in between* the cavities. In SL3, the distance between neighboring cavities in the X direction is 1.44 μm, so when light is centered on one cavity, the intensity at a neighboring cavity is low, less than 15% (see Fig. 10), hence a neighboring cavity is only weakly excited. We image the sample surface with an unfocused LED to precisely align the incident spot relative to each defect pore.

III. RESULTS

A. Spectral features of superlattice bands

Figure 3 shows representative reflectivity and lateral scattering spectra for two main situations, namely *on* a cavity [Figs. 3(a) and 3(c)] and in between [Figs. 3(b) and 3(d)] [46]. Since the 3.4-μm distance between two cavities is much greater than the Bragg length ($L_B = 0.33 \pm 0.07$ μm, see Appendix E), spectra collected in between cavities effectively correspond to probing the unperturbed crystal. In both cases,

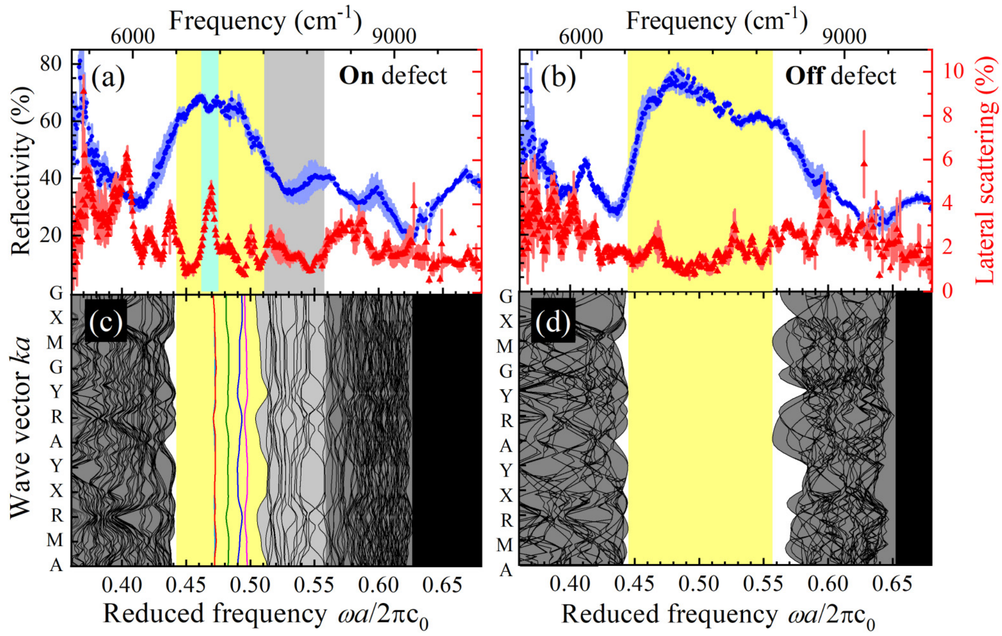

FIG. 3. [(a) and (b)] Measured reflectivity (blue dots) and lateral scattering (red triangles, right ordinate) of cavity superlattice SL5 on a defect and in between two defects ($X = 2.5$ μm) for s polarization. The broad reflectivity peaks correspond to band gaps at the particular location as shown by the yellow regions that match very well with theory. The lateral scattering peak at 6900 cm^{-1} in the band gap [cyan highlight in (a)] corresponds to a reflectivity trough and a Cartesian band in the band structures. (c) Photonic band structure of a $3 \times 3 \times 3$ cavity superlattice with frequency and wave vector reduced by lattice parameter a. The yellow region between $a/\lambda = 0.44$ and 0.502 is the 3D photonic band gap of the superlattice, and allowed bands outside the gap are shown as dark gray areas. The cavity superlattice sustains two types of bands in the band gap: flat bands typical of Cartesian light in the lower half of the gap (colored bands), and others in the upper half of the gap (black bands). (d) Photonic band structure of an inverse woodpile photonic crystal with $r/a = 0.22$ without cavities. For ease of comparison, the high symmetry points here also correspond to a $3 \times 3 \times 3$ supercell. The yellow region between $a/\lambda = 0.44$ and 0.56 is the unperturbed 3D band gap.

we observe an intense and broad reflectivity peak that corresponds to the 3D band gap of the crystal, as previously observed in crystals without intentional defects [44,47]. While common lore has it that an increased number of defects in a photonic crystal adversely influences a band gap, ultimately even closing it [48–50], we see here that the introduction of a superlattice of defects does *not* close the band gap, and hence the superlattice modes identified below are indeed confined by a 3D band gap.

To identify reflectivity features in Fig. 3(a), we compare the measurements with the band structures in Fig. 3(c), computed for a cavity superlattice with pore radii corresponding to those obtained at the probing location using the method [51] from Ref. [44]. The band structure shows that the cavity superlattice sustains two types of bands inside the 3D band gap, namely flat defect bands typical of Cartesian light, and other dispersive bands in the upper half of the band gap [23]. Due to the appearance of the dispersive bands, the band gap of the cavity superlattice structure shown in Fig. 3(a) is markedly narrower than the unperturbed band gap shown in Fig. 3(b). This is clearly observed in the superlattice spectra, where a broad trough near 7800 cm^{-1} coincides with the dispersive bands in the upper half of the original band gap, and thus narrows the superlattice band gap [52]. The center frequency and the width of the measured reflectivity band gap of the superlattice [see Figs. 3(a) and 3(b)] agree very well with the theoretical band gap [see Figs. 3(c) and 3(d), respectively], which highlights that the fabricated nanostructure and its optical functionality match closely with the designed structure and the intended optical behavior. We also observe that on focusing the incident light on the cavity, the maximum reflectivity $R_{\max} = 68\%$ [see Fig. 3(a)] is less than when focusing away from the cavities where the maximum is $R_{\max} = 74\%$ [see Fig. 3(b)], which is reasonable since the light incident on cavities is also scattered nonresonantly, thereby reducing the specular reflectivity. This observation is reproduced at other cavity and crystal locations by scanning in the Y direction, see Appendix F.

When focusing on a cavity, the lateral scattering spectrum shows a distinct peak at 6900 cm^{-1} within the band gap, see Fig. 3(a). The peak represents light scattered from incident wave vectors $\mathbf{k}_{\rm in}$ to outgoing wave vectors $\mathbf{k}_{\rm out}$ in completely different directions than either the incident ones ($\mathbf{k}_{\rm out} \neq \mathbf{k}_{\rm in}$) or their Bragg diffracted counterparts ($\mathbf{k}_{\rm out} \neq \mathbf{k}_{\rm in} + \mathbf{G}$). Therefore, we expect less light to be reflected and, indeed, the reflectivity spectrum reveals a corresponding trough in the same frequency band. Moreover, the lateral scattering peak and the reflectivity trough match well with a Cartesian superlattice band in the band structures, see Fig. 3(b). We verified that the scattering peak differs from random speckle that is also observed, see Fig. 13. The observation of resonant features both in specular reflectivity and in scattering confirms that the confinement of light in the superlattice is truly a 3D phenomenon, as opposed to 1D confinement in a Fabry-Pérot cavity that would be apparent in reflectivity but not in lateral scattering. We emphasize that the peak only appears when incident light is focused onto a defect; when incident light is

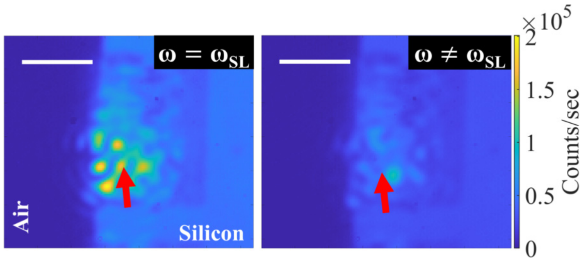

FIG. 4. Camera images of the XY-front surface of superlattice SL3 for cross-polarized light on a common intensity scale at two frequencies: $\omega = 7386\ \mathrm{cm}^{-1} = \omega_{\mathrm{SL}}$ (left, center of superlattice peak) and $7174\ \mathrm{cm}^{-1}$ (right, outside superlattice peak). The surface of the crystal is illuminated by a separate LED. The white scale bar indicates 5 μm (top left). The red arrow in each panel points to the incident focus that was kept constant while scanning frequency.

focused in between defects the peak is absent, see Fig. 3(b). Hence we conclude that the scattering peak corresponds to a Cartesian superlattice band [53].

B. Hopping in the X and Z directions

To visualize the hopping of light in the superlattice, we capture images of the front surface of SL3 while varying the frequency. We detect crossed polarized light to select the light that has multiply scattered inside the crystal and suppress single scattering from the sample surface [54]. Hence, we expect to detect both light scattered from the cavities and from unavoidable disorder. Figure 4 presents images for two frequencies ω, tuned to the center of the superlattice peak $\omega = \omega_{\mathrm{SL}}$ $(=7386\ \mathrm{cm}^{-1})$, and detuned to $\omega \neq \omega_{\mathrm{SL}}$ $(=7174\ \mathrm{cm}^{-1})$, within the unperturbed original band gap. In both cases, we see a speckle pattern due to multiple scattering by unavoidable imperfections [50]. A remarkable observation is that at $\omega = \omega_{\mathrm{SL}}$, the light spreads over a large area, much larger than the incident spot. Intensity maxima near the defect pores are observed, as shown in the left image in Fig. 4. In the X direction, the three intensity maxima are equally spaced with an average distance of 1.50 ± 0.06 μm that agrees well with the designed cavity distance $c_{\mathrm{SL}} = 3c = 1.44$ μm. The good agreement proves that in SL3 the superlattice frequency hops over at least three neighboring cavities, which firmly establishes that we observe Cartesian light hopping in a 3D photonic band gap cavity superlattice. Conversely, when we probe the same location on the crystal at an off-resonant frequency $(\omega \neq \omega_{\mathrm{SL}})$ (Fig. 4, right), we observe a faint single spot typical of light localized in a single uncoupled cavity. Moreover, the intensity is brighter on resonance (left) compared to off-resonance (right), further confirming that light is transported by coupled cavity modes, in other words, the superlattice band.

C. Hopping in the third dimension: Y direction

Due to an inadvertent nanofabrication inhomogeneity of the underlying band gap crystal (seen before in Ref. [44]), we observe in position-dependent measurements that the band gap shifts across the crystals, as shown in the Y scan in Figs. 5(a) and 5(b). In superlattice SL5 [Fig. 5(a)], we observe near the second defect pore a scattering resonance centered at $6896\ \mathrm{cm}^{-1}$. Scanning onward to the third defect pore, a different cavity resonance appears at a distinct, lower frequency $6358\ \mathrm{cm}^{-1}$, shifting in the same sense as the (local) photonic band gap. Since the peaks differ for the different defects, the cavities are uncoupled. On the other hand, in superlattice SL3 the scattering peak has the same constant center frequency $7386\ \mathrm{cm}^{-1}$ when scanned across multiple cavities and also in between [see Fig. 5(b)], which is striking in view of the marked shift of both band edges. The observations in Fig. 5 are not affected by "smearing" by a relatively large beam spot, since Fig. 5(a) reveals abrupt jumps between different cavities, and Fig. 5(a) reveals sharp changes of the high-frequency band gap edge. Hence, for superlattice spacing $a_{\mathrm{SL}} = 3a$, multiple cavities are coupled, and the peak at $7386\ \mathrm{cm}^{-1}$ represents a *bona fide* superlattice band typical of Cartesian light that hops through the superlattice [22]. To the best of our knowledge, this is the first experimental observation of 3D discretized light transport in a cavity superlattice.

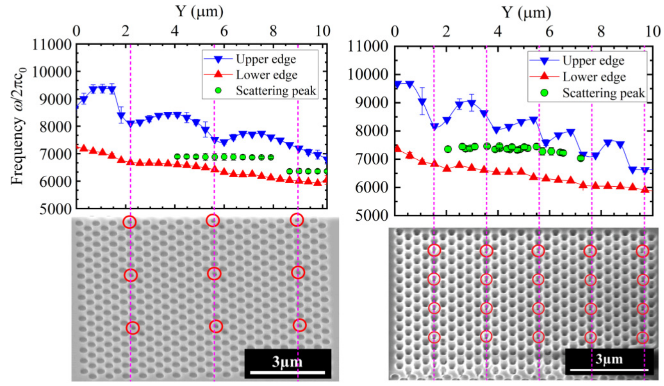

FIG. 5. Lower (red triangles) and upper band edges (blue downward triangles) of the position-dependent photonic gap versus Y, from reflectivity measured on SL5 (left) and SL3 (right). The lateral scattering peaks in the gap are shown by green circles. SEM images of the same crystals are stitched below with the same scale, where magenta dashed lines trace the positions of the cavities.

IV. DISCUSSION

In pursuit of 3D Anderson localization of light in 3D [30], we propose that an interesting approach is the analogy with Anderson's original work namely impurities in crystals [55]. Since cavities are known to induce impurity states in a photonic band gap [56], a variation of the individual cavities' resonance frequency and a variation of their intercavity hopping rates correspond to diagonal and off-diagonal disorder in the Anderson model, respectively. The amount of diagonal and off-diagonal disorder can be readily controlled by introducing intentional variations in the cavity pore radii and in their locations within the unit cell during the fabrication of the 3D photonic crystals.

Pioneering work by Rinne *et al.* and Ishizaki *et al.* has shown that guiding light along 3D waveguides confined in a 3D band gap is feasible, leading to the injection and detection of light in out-of-plane directions and to light being bent around sharp corners using linear defects [57,58]. Although light is also readily guided along coupled cavities [15], a system of 3D coupled cavities confined by a 3D band gap as demonstrated here offers a new manner to guide light in 3D by hopping from cavity to cavity, as illustrated in Fig. 1. A 3D cavity superlattice offers as a novel feature the opportunity to tune the coupling efficiencies in different directions.

For future applications such as 3D photonic network with potentially more degrees of control than ready-made networks [59], we propose to add phase control to the waves hopping in 3D from cavity to cavity, e.g., by wavefront-shaping tools [60]. Hence, light can take a subset of all possible paths, one example being illustrated in Fig. 1, and thereby one obtains control on how ("which path") and where ("which cavity") the light travels. One could employ wavefront control to selectively guide light, for instance, to exit at the lateral face of the crystal [61]. Since photonic control is nowadays feasible down to single photons [62], the notion above could find application in 3D quantum networks with significant network size scaling advantages compared to conventional 2D networks with opportunities in analog quantum simulation [27–29] in addition to classical application for 3D laser cavities [63].

ACKNOWLEDGMENTS

We thank Cornelis Harteveld for expert technical help and crystal nanofabrication, Chris Toebes for help with the setup, and Ad Lagendijk for valuable insights. We thank Arie den Boef, Patrick Tinnemans, Vahid Bastani, Wim Coene, and Scott Middlebrooks from ASML for insightful discussions on data analysis and Bill Barnes (Exeter, COPS) for proposing the notion Cartesian light. W.L.V. dedicates this paper to the memory of Costas Soukoulis, who co-invented the inverse woodpile structure and provided much encouragement over many years. This research is supported by NWO-Toegepaste en Technische wetenschappen (TTW) Perspectief program P15-36 "Free-form scattering optics" (FFSO) in collaboration with TU Delft, TU Eindhoven, and industrial users ASML, Demcon, Lumileds, Schott, Signify, and TNO.

APPENDIX A: PHOTONIC BAND GAP CAVITY SUPERLATTICE AND CARTESIAN LIGHT

Let us conceive of a 3D superlattice of coupled resonant cavities that are embedded in a 3D photonic band gap crystal [22]. Using a combination of plane-wave expansion and finite-size scaling methods, as well as machine learning [22–24], it has been realized that light (or vector electromagnetic) waves reveal an unconventional way of propagation that differs radically from well-known conventional 3D spatially extended Bloch wave propagation in crystals, from light tunneling through a band gap [34,64], from coupled-resonator optical waveguiding [15], and also from light diffusing at the edge of a gap [65]. We have computed the dispersion relations of the 3D cavity superlattice with the cubic inverse woodpile structure that is amenable to CMOS-compatible 3D silicon nanofabrication [38,39,66,67]. Many new bands appear in the band gap of the original perfect (unperturbed) 3D photonic band gap crystal, see also Fig. 3. Several of the new bands reveal a dispersion bandwidth that is significantly larger in the certain high-symmetry directions than in other directions. To explain the directionality of the dispersion bandwidth, we invoke the tight-binding method from which we derive coupling coefficients in all three dimensions.

When viewed in a hopping picture, we find that light hops predominantly in a few high-symmetry directions including the Cartesian (x, y, z) directions, hence the name "Cartesian light" was proposed. Hopping is considered to proceed from a certain starting cavity to a nearest-neighbor or perhaps next-nearest-neighboring cavity (if the relevant hopping rate is sufficiently large.) No hopping is considered in other, oblique, directions for the simple reason that there are no neighboring cavities located.

When an ideal single plane wave of light is used to excite the superlattice, then a single state with a well-defined wave vector $\mathbf{k}$ of the superlattice band is excited (see also Fig. 3 of the main text). When exciting externally with focused light, as in our experiment, it is reasonable that a continuum of states with a continuum of wave vectors is excited.

In the theoretical descriptions to date of Cartesian light by Hack *et al.* and Kozon *et al.* [23,24], the transport is described in steady state. Conversely, hopping may be interpreted in the time domain (typically discussed in words like: "a photon starts at cavity 1 at t_1 and hops to cavity 2 at time t_2"), but this is not the case in the transport theories above.

APPENDIX B: INVERSE WOODPILE CRYSTAL STRUCTURE, CAVITY DESIGN, AND COMPUTATIONS

To create a resonant cavity in an inverse woodpile photonic crystal, Woldering *et al.* proposed a design whereby two proximal perpendicular pores have a smaller radius ($r' < r$) than all other pores, as shown in Fig. 6(a) [45]. This structure has a tetragonal crystal symmetry, with the Brillouin zone and its high-symmetry path depicted in Fig. 7. Near the intersection region of the two smaller pores, the light is confined in all three directions within a mode volume as small as $V_{\text{mode}} = \lambda^3$ where λ is the free-space wavelength [45]. Supercell band structures reveal up to five resonances within the band gap of the perfect crystal, depending on the defect pore radius r' [45]. The best confinement occurs for a defect radius $r'/r = 0.5$ that is also considered here.

Figure 6(b) shows a 3D superlattice of cavities as is studied here, where each sphere indicates one cavity, as shown in Fig. 6(a). The cavity superlattice has lattice parameters (c_s^x, a_s, c_s^z) in the (x, y, z) directions that are integer multiples of the underlying inverse woodpile lattice parameters: $c_s^x = M_x c$, $a_s = M_y a$, $c_s^z = M_z c$. Here we study the $M_x \times M_y \times M_z = 3 \times 3 \times 3$ superlattice such that the cavities are repeated every three unit cells with lattice parameters $c_s^x = 3c$, $a_s = 3a$, $c_s^z = 3c$. Thus, the cavity superlattice is also cubic, similar to the underlying inverse woodpile structure.

We have calculated the band structure of the 3D cavity superlattice using the plane-wave expansion method [21,34], implemented in version 1.5 of the MIT photonic bands (MPB) code [69]. We employ the grid resolution $48 \times 68 \times 48$ per unit cell of the superlattice. The silicon backbone is modeled with a dielectric function equal to $\epsilon = 12.1$, as also used previously [22,23,70]. The band structures shown in Fig. 3(c) of the main paper were computed for reduced radius $r/a = 0.22$ of the underlying inverse woodpile crystals and for defect pores with reduced pore radii $r' = r/2$. All calculations were

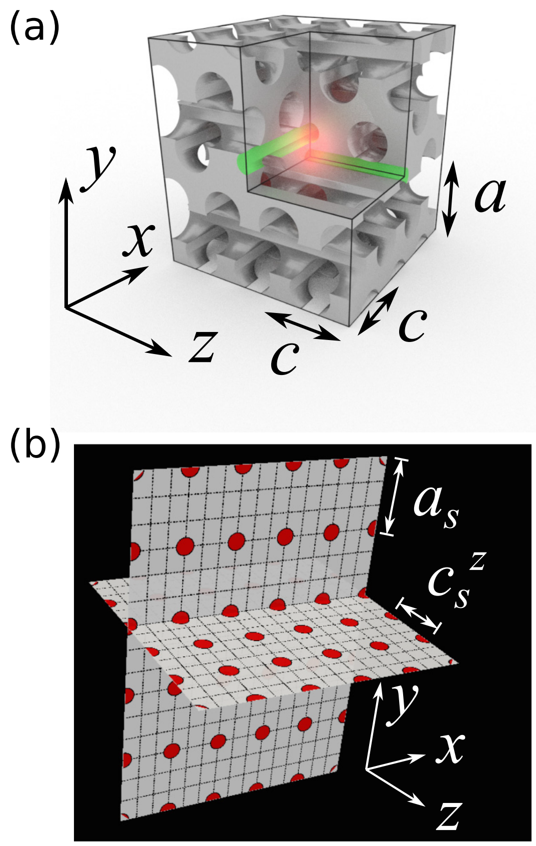

FIG. 6. (a) Design of a single cavity in an inverse woodpile photonic band gap crystal shown in a cutout of a $M_x \times M_y \times M_z = 3 \times 2 \times 3$ supercell that is surrounded by boxed lines. The high-index backbone is shown in gray. Two proximal smaller defect pores are indicated in green, and the cavity region is highlighted as the bright region at the center. The tetragonal lattice parameters a and c are shown, as well as the x, y, z coordinate system. (b) (x, z) and (x, y) cross sections through a 3D superlattice of resonant cavities, with red circles indicating cavities and dashed rectangles representing unit cells of the underlying inverse woodpile crystal structure [see panel (a)]. The lattice parameters (c_s^x, a_s, c_s^z) of the superlattice are shown, as well as the x, y, z coordinate system.

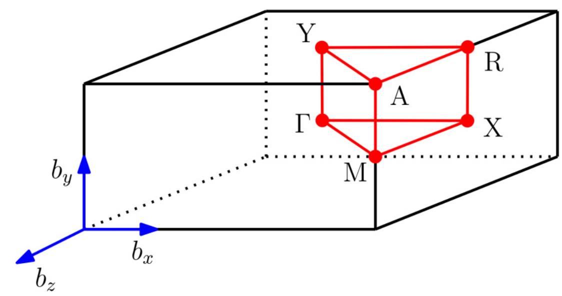

FIG. 7. Brillouin zone of a tetragonal unit cell (black) with the corresponding high-symmetry path (red). The Cartesian basis vectors (blue) are denoted by b_x, b_y, b_z. For more details, see Ref. [68].

performed on the "Serendipity" cluster in the MACS chair at the MESA$^+$ Institute.

APPENDIX C: OPTICAL SETUP

We have developed a versatile near-infrared setup to collect position-resolved broadband reflectivity and lateral scattering spectra of photonic nanostructures, see Fig. 8. The setup has a spectral range from 5300 to 11 000 cm^{-1} (or wavelengths $910 < \lambda < 1880$ nm) in the NIR and SWIR to be compatible with silicon nanophotonics. The setup is a realization of the setting schematically depicted in Fig. 1 of the main paper. We aim to inject light at a specific location on the crystal's front surface and detect light exiting from a different surface. Hence, we employ a focused beam and collect lateral scattering, as depicted in Fig. 1.

All measurements are processed in LabView environments. The near-infrared range of operation is compatible with 3D silicon nanophotonics as it avoids intrinsic silicon absorption. A pictorial representation of the full optical setup is shown in Fig. 8. The setup consists of three main components:

(i) a broadband tunable coherent source,
(ii) a broadband wavefront shaper, and
(iii) twin-arm imaging of reflected and lateral (YZ plane) scattered signals from the sample.

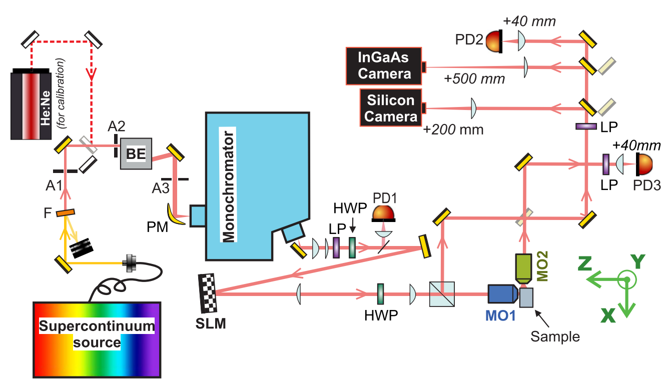

FIG. 8. Optical setup to measure position-resolved microscopic broadband reflectivity, lateral scattering and wavefront shaping. The Fianium SC is the broadband supercontinuum source, the long-pass glass filter F blocks the visible light at $\lambda < 850$ nm, the BE is a reflective beam expander. The monochromator filters the light to a narrow band with a linewidth of about 0.7 nm. The linear polarization of the incident light is set by a half-wave plate (HWP, $\lambda/2$), and LP are linear polarizers to analyze the light. The SLM is a spatial light modulator suited for wavefront shaping (not done here) and for correcting the direction of incoming light onto the sample. Incident light is focused on the sample with a 100× objective MO1 (NA = 0.85) that also collects the reflected light. Objective MO2 (NA = 0.42) collects light scattered from the sample in the perpendicular lateral ($-X$) direction that is detected by photodiode PD3. The NIR camera (InGaAs) views the sample in reflection with an effective magnification of 250×. The other Silicon camera can also be used to view the sample when using shorter wavelengths. Photodiode PD1 monitors the incident light power, and PD2 and PD3 measure reflected and scattered signals from the crystal, respectively. The sample is mounted on a three-axis precision stage to adjust focusing and to focus input light to targeted positions. The coordinates are shown on the sample, where incident light is along $-Z$ direction and the lateral scattered light exits from the YZ surface.

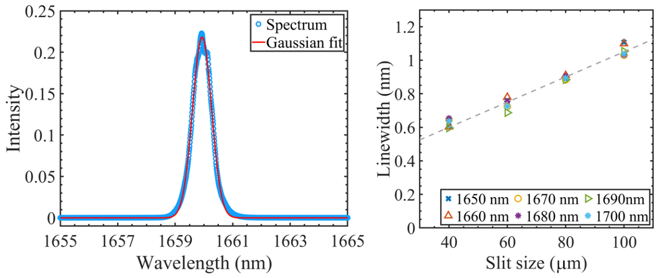

FIG. 9. Left: The output spectrum of the monochromator for one single wavelength ($\lambda = 1660$ nm or $\omega_c = 6024$ cm^{-1}) measured by a separate spectrometer. The linewidth is estimated by modeling with a Gaussian and taking the full width at half maximum (FWHM), yielding 0.78 nm or $\delta\omega = 2.83$ cm^{-1}, for a monochromator slit width of 60 μm. Right: The linewidth of the source versus slit width of the monochromator output at six different wavelengths, which is linearly proportional. In all experiments, the width was set at 50 μm.

The reflectivity part has been described earlier in Ref. [44]. The broadband tunable coherent source is realized by spectrally filtering the emission from a supercontinuum source (Fianium SC 450-4, 450–2400 nm) with a monochromator (Oriel MS257; 1200 lines/mm grating). A long-pass filter (cut-off wavelength 850 nm) is used to reject the background from second-order diffraction of shorter wavelengths. The filtered light beam is expanded in a reflecting beam expander (Thorlabs) and sent to a parabolic mirror (PM) to focus the light to fit through the input slit of the monochromator, see Fig. 8. The monochromator scans optical frequencies ranging from 4700 to 11 000 cm^{-1} (or wavelengths $900 < \lambda < 2120$ nm) with a linewidth of 0.6 ± 0.1 nm exiting from the output slit of width 50 μm, see Fig. 9, and a tuning precision better than 0.2 nm. Since we use this setup also for wavefront shaping [61], we use sequential scanning of wavelengths instead of measuring the spectrum at once with a spectrometer as in Refs. [47,71,72]. A He:Ne laser is used to calibrate the grating of the monochromator. The filtered light is then collimated and expanded to a beam diameter of 7.5 mm. A small fraction (8%) of the light is sent to a photodiode PD1 using a glass plate as a reference to monitor the input power. The main beam is incident on a reflective phase-only spatial light modulator (Meadowlark optics; 1920×1152 pixels; AR coated: 850–1650 nm). Since the output of the source is randomly polarized, a linear polarizer (LP) followed by a half-wave plate (HWP) are placed at the monochromator output to select the desired linear polarization orientation.

The s-polarized light on the superlattice is defined to have the E-field perpendicular to the X-directed pores.

APPENDIX D: NEAR-INFRARED REFLECTIVITY AND LATERAL SCATTERING

In our optical setup shown in Fig. 8, the sample is mounted on an XYZ translation stage that has a step size of about 30 nm. The reflected light from the SLM is sent to an infrared apochromatic objective (Olympus LC Plan N 100×) to focus the light onto the sample's surface with a numerical aperture NA = 0.85. For spectral measurements the SLM is used to reflect as a flat mirror, and in addition, the SLM is also used to correct for a slight wavelength-dependent beam tilt. The waist of the beam reflected from the SLM is narrowed and recollimated by a pair of lenses to fill the back aperture of the objective.

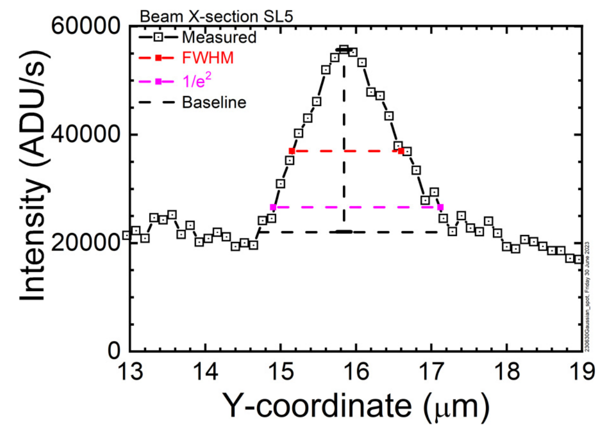

FIG. 10. Cross section of the laser focus obtained from a camera image (as in Fig. 4) at $\lambda = 1400$ nm. The vertical dashed line indicates the peak position, the black horizontal line is the baseline, the magenta dashed line is the $1/e^2$ intensity level, and the red dashed line the full width at half maximum (FWHM).

Using Gaussian optics for the position intensity distribution $I(x, y)$, the beam waist in the focus (at $1/e^2$ intensity level) is equal to $w = 1.05$ μm, see Fig. 10. So when we focus on one cavity, see Fig. 4, the relative intensity at a neighboring cavity in the SL3 superlattice—corresponding to three lattice parameters away in the x direction, or $\Delta x = 3c = 1.44$ μm—is only:

$$I(\Delta x) = \exp^{-(\Delta x/w)^2} = \exp^{-(1.37^2)} = 0.15 = 15\%. \quad \text{(D1)}$$

Thus, when we focus on one cavity, as in Fig. 4, a neighboring cavity is hardly excited. Therefore, we conclude that in Fig. 4 (left) the light being emitted by multiple cavities means that they are coupled and not accidentally excited by an extended beam. For comparison, Fig. 4 (right) shows that in absence of coupling, only one cavity is seen in the camera image.

A second HWP is introduced on the beam path before the objective to rotate the linear polarization of the incident light on the sample for polarization-dependent measurements.

Light reflected by the sample is collected by the same objective and a beam splitter directs the reflected light towards the detection arm where the reflection from the sample is imaged onto an IR camera (Photonic Science InGaAs). In order to locate the focus of the input light on the surface, a NIR LED is used to illuminate the sample surface. We use the XYZ translation stage to move the sample to focus the light on the desired location. For example, an image of a 3D crystal as seen on the IR camera reveals the XY surface of the Si beam, see for example Fig. 4 in the main paper. The bright circular spot with a diameter of about 2 μm is the focus of light reflected from the crystal. The rectangular darker areas of about 8×10 μm are the XY surfaces of the 3D photonic crystals. They appear dark compared to the surrounding silicon since the LED illumination is outside the band gap of these crystals whose effective refractive index is less than that of silicon.

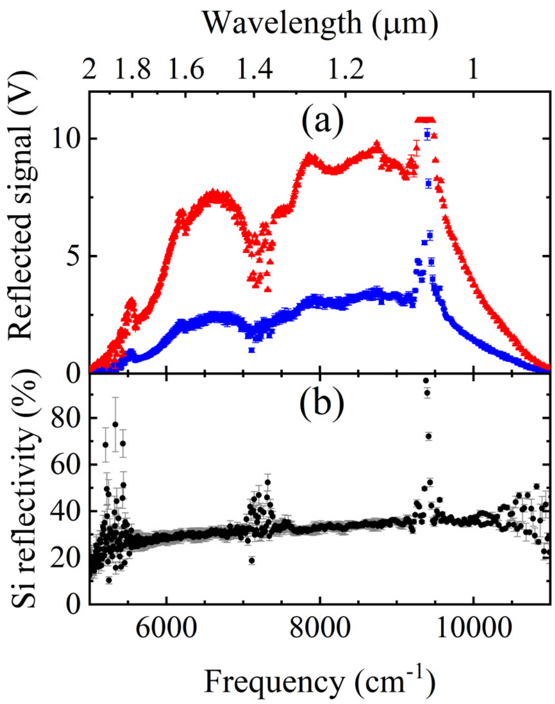

FIG. 11. (a) Raw spectra recorded by photodiode PD2 of light reflected from a gold mirror (red triangles) and a clean silicon substrate next to the photonic crystals (blue squares). Due to the very high power near the pump frequency 9400 cm^{-1} of the supercontinuum source, the intensity is usually saturated, hence this range is disregarded in our analysis of the measurements. (b) Reflectivity of bulk Si normalized to the gold reflectivity.

Once the input light beam is focused on the sample, the reflected light is sent to photodiode PD2 (Thorlabs InGaAs DET10D/M, 900–2600 nm) by flipping out the mirror in front of the camera. The photodiode records the reflected intensity I_R as the monochromator scans the selected wavelength range. At the same time, the scattered light from the sample in the lateral direction is collected by a long working distance apochromatic objective MO2 (NA = 0.42) and sent to a third photodiode PD3 (similar as PD2). An analyzer in front of each photodiode is used to select either parallel or cross polarization of the reflected and scattered light with respect to the input. Thus, in total we collect two sets of spectra as signal every time the wavelengths are scanned through the desired range: a reflectivity spectrum, and a lateral scattering spectrum. By moving the sample stage in the Y direction, the focus is scanned across the crystals with a step size of about 0.4 μm, resulting in typically 30 reflectivity and lateral scattering spectra per scan. The raw reflectivity measured on two reference samples, viz., a clean gold mirror and the bulk silicon substrate are shown in Fig. 11(a). The spectra show that the intensity of the supercontinuum source varies markedly with frequency, hence proper referencing is important. The intensity cutoff at high frequencies is mainly due to limited detection bandwidth of the InGaAs photodiode and the cutoff at low frequencies is due to the absorption by the refractive optics (lenses, objectives, wave plates) and the limited bandwidth of the supercontinuum source. The range of noisy data near 7000 cm^{-1} is attributed to water vapor absorption that may vary from day-to-day depending on laboratory conditions and on the weather. Hence care is exerted while analyzing data in this wavelength range, by using data obtained in a narrow time window. In future, the noise may be suppressed by placing the setup in box purged with dry air or nitrogen. The intense peak at 1064 nm is the pump wavelength of the supercontinuum source; due to unavoidable detector saturation near this peak, data in this range is typically removed from the analysis. Recording a typical reflectivity or lateral scattering spectrum takes about 5 to 25 min, depending on the chosen wavelength step size (typically 10 nm or 2 nm). The calibrated reflectivity and lateral scattering are defined as

$$R \equiv I_R/I_{0R}, \tag{D2}$$

$$LS \equiv I_{LS}/I_{0LS}. \tag{D3}$$

For reflectivity, the spectral response I_R of the samples is referenced to the signal I_{0R} reflected from a clean gold mirror that reflects 96%. Since it is tedious to dismount and realign the sample to take reference spectra during long measurements on crystals on a silicon beam, we also take secondary reference measurements on bulk silicon outside the crystals, which has a flat response $R \approx 31\%$ with respect to the gold mirror. The bulk silicon reflectivity is plotted in Fig. 11(b) that agrees with the expected $\approx$31% reflectivity of Si for normal incidence in the NIR spectral region [73]. The spectrum is flat [74] without any features apart from the noise discussed above. Therefore, we use the Si signal also as a reference for reflectivity measurements.

Obtaining a reference for lateral scattering is a bit tricky, since we need to send the input signal travel through the objective MO2 for correct referencing, see Fig. 8. Therefore, we used the edge of a silicon beam that was cut at 45° to reflect the incoming light coming through MO1 towards MO2 and send it to PD3, just like the lateral scattering signal. Using Fresnel reflectivity of 45° incident light on silicon, we use a calibration of $R_p = 43\%$ reflectivity for s-polarized light and $R_p = 19\%$ reflectivity for p-polarized light. To ensure that the signal to noise ratio of the photodiode response is sufficient to detect signal in the desired range, each detector photodiodes are fed into a lock-in amplifier to amplify the signal with a suitable gain. Since a serial measurement mode holds the risk of possible temporal variations in the supercontinuum source, we simultaneously collect the output of the monochromator with photodiode PD1 in each reflectivity scan. An example of reference spectra for LS measurements is shown in Fig. 12 for two orthogonal polarizations of the incident light. All measurements described above are controlled by and the data saved by a home-built LabVIEW program, that also allowed for remote control, which turned out to be very convenient when access to our laboratories was restricted during the Covid pandemic.

APPENDIX E: BRAGG LENGTH

The Bragg length L_B is the characteristic length scale of the exponential decay of the intensity of an incident beam of waves with a frequency inside a photonic gap [75–77]. The Bragg length is the inverse of the imaginary part of the wave vector $\mathbf{k}$: $L_B(\omega) = 1/(\mathbb{I}\mathrm{m}(\mathbf{k})(\omega))$ and depends on

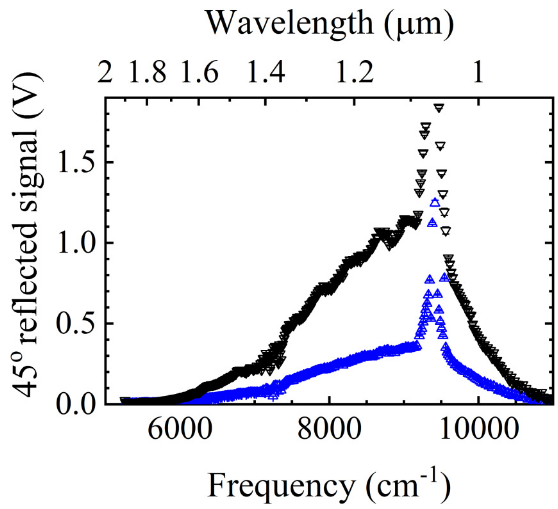

FIG. 12. Raw spectra recorded by photodiode PD3 of light reflected at 45° incident from a silicon surface for s polarization (black downward triangles) and p polarization (blue upward triangles).

frequency ω throughout the gap. The frequency dependence of the imaginary part of the wave vector in a stop gap is known to be parabolic [78], vanishing at the band edges and maximal at the gap center. For 3D inverse woodpile crystals made from silicon, as studied here, the Bragg length at the band gap center has been computed by Devashish *et al.* to be $L_B = 0.2$ μm, corresponding to $\mathbb{I}\mathrm{m}(\mathbf{k}) = 5\ \mu\mathrm{m}^{-1}$ [79]. From the parabolic frequency dependence of the imaginary wave vector, we interpolate at the superlattice band frequency [cyan band in Fig. 3(a)] that $\mathbb{I}\mathrm{m}(\mathbf{k}) = 3.7\ \mu\mathrm{m}^{-1}$, and hence $L_B = 0.27$ μm. From a similar reasoning for the superlattice (with a narrower band gap, see Fig. 3, yet here the superlattice band is at the gap center), we arrive at $\mathbb{I}\mathrm{m}(\mathbf{k}) = 2.5\ \mu\mathrm{m}^{-1}$, and hence $L_B = 0.4$ μm. It is reasonable that the Bragg length is bounded by these estimates, and hence $L_B = 0.33 \pm 0.07$ μm. This is much less than the distance between the cavities in the superlattice, hence probing the crystal in between cavities is a reasonable approximation of an unperturbed reference crystal.

APPENDIX F: DISTINGUISHING SUPERLATTICE SCATTERING FROM RANDOM SPECKLE

To distinguish a superlattice peak from random speckle peaks [80,81] that arise as a result of random and unavoidable structural variations [50], we monitor the reproducibility of the peaks while scanning the illuminating spot across the sample surface. Therefore, we plot multiple lateral scattering spectra at different Y positions near the defect pore at $X = 2.5$ μm, as shown in Figs. 13(a) and 13(b) for the superlattices SL5 and SL3, respectively. It is clearly apparent that the peak near 6900 cm^{-1} reproduces at all positions near the defect pore, with gradually decreasing intensity as the focus moves away from the defect pore. We also observe a second reproducing peak near 7386 cm^{-1}, possibly a second superlattice band. For superlattice SL3 [Fig. 13(b)], we also see a scattering peak near 7386 cm^{-1} that reproduces even across multiple defect pores. All other scattering peaks do not reproduce, hence they are uncorrelated speckle arising from unavoidable disorder of the crystal. Therefore, we conclude that all reproducing peaks are spectral features of the intentional superlattice of defects.

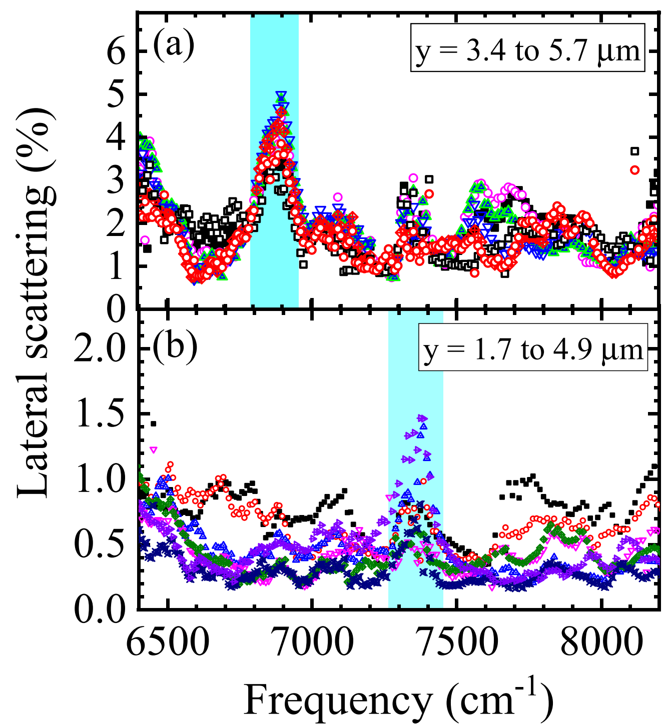

FIG. 13. (a) Multiple lateral scattering spectra collected on superlattice SL5 at different y positions in the vicinity of a defect show that the peak near 6900 cm^{-1} is reproducible, whereas other peaks do not reproduce and are hence identified as random speckle. (b) Multiple spectra across three defect pores, show a reproducible peak near 7386 cm^{-1} for superlattice SL3. The Y positions of the spectra are given in the legends while the X position is nearly constant ($X \approx$ 2.5 μm). The frequency range shown covers the original band gap of the unperturbed crystal (see also Ref. [44]).

[1] *Analogies in Optics and Micro Electronics*, edited by W. van Haeringen and D. Lenstra (Springer, Dordrecht, 1990).

[2] *Photonic Crystals and Light Localization in the 21st Century*, edited by C. Soukoulis (Springer, Netherlands, 2001).

[3] P. Sheng, *Introduction to Wave Scattering, Localization and Mesoscopic Phenomena* (Springer Verlag, Berlin, 2006).

[4] E. Akkermans and G. Montambaux, *Mesoscopic Physics of Electrons and Photons* (Cambridge University Press, Cambridge, UK, 2007).

[5] V. V. Kruglyak, S. O. Demokritov, and D. Grundler, Magnonics, J. Phys. D **43**, 264001 (2010).

[6] M. Ghulinyan and L. Pavesi, *Light Localisation and Lasing: Random and Pseudo-random Photonic*

Structures (Cambridge University Press, Cambridge, UK, 2015).
[7] G. Feher and A. F. Kip, Electron spin resonance absorption in metals. I. Experimental, Phys. Rev. **98**, 337 (1955).
[8] W. L. Bragg and E. J. Williams, The effect of thermal agitation on atomic arrangement in alloys, Proc. Royal Soc. Lond. Ser. A **145**, 699 (1934).
[9] H. A. Bethe, Statistical theory of superlattices, Proc. Royal Soc. Lond. Ser. A **150**, 552 (1935).
[10] J. Li, M. Chong, J. Zhu, Y. Li, J. Xu, P. Wang, Z. Shang, Z. Yang, R. Zhu, and X. Cao, 35% efficient nonconcentrating novel silicon solar cell, Appl. Phys. Lett. **60**, 2240 (1992).
[11] A. Luque and A. Martí, Increasing the efficiency of ideal solar cells by photon induced transitions at intermediate levels, Phys. Rev. Lett. **78**, 5014 (1997).
[12] C. Tablero, P. Palacios, J. J. Fernández, and P. Wahnón, Properties of intermediate band materials, Sol. Energy Mater. Sol. Cells **87**, 323 (2005).
[13] J. T. Sullivan, C. B. Simmons, J. J. Krich, A. J. Akey, D. Recht, M. J. Aziz, and T. Buonassisi, Methodology for vetting heavily doped semiconductors for intermediate band photovoltaics: A case study in sulfur-hyperdoped silicon, J. Appl. Phys. **114**, 103701 (2013).
[14] Q. Liu, Z. Cai, D. Han, and S. Chen, Natural intermediate band in I_2-II-IV-VI_4 quaternary chalcogenide semiconductors, Sci. Rep. **8**, 1604 (2018).
[15] A. Yariv, Y. Xu, R. K. Lee, and A. Scherer, Coupled-resonator optical waveguide: A proposal and analysis, Opt. Lett. **24**, 711 (1999).
[16] M. Bayindir, B. Temelkuran, and E. Ozbay, Propagation of photons by hopping: A waveguiding mechanism through localized coupled cavities in three-dimensional photonic crystals, Phys. Rev. B **61**, R11855 (2000).
[17] H. Altug and J. Vučković, Photonic crystal nanocavity array laser, Opt. Express **13**, 8819 (2005).
[18] J. Ma, L. J. Martínez, S. Fan, and M. L. Povinelli, Tight-binding calculation of radiation loss in photonic crystal crow, Opt. Express **21**, 2463 (2013).
[19] S. Olivier, C. Smith, M. Rattier, H. Benisty, C. Weisbuch, T. Krauss, R. Houdré, and U. Oesterlé, Miniband transmission in a photonic crystal coupled-resonator optical waveguide, Opt. Lett. **26**, 1019 (2001).
[20] N. Matsuda, E. Kuramochi, H. Takesue, and M. Notomi, Dispersion and light transport characteristics of large-scale photonic-crystal coupled nanocavity arrays, Opt. Lett. **39**, 2290 (2014).
[21] N. W. Ashcroft and N. D. Mermin, *Solid State Physics* (Holt, Rinehart & Winston, New York, 1976).
[22] S. A. Hack, J. J. W. van der Vegt, and W. L. Vos, Cartesian light: Unconventional propagation of light in a three-dimensional superlattice of coupled cavities within a three-dimensional photonic band gap, Phys. Rev. B **99**, 115308 (2019).
[23] M. Kozoň, A. Lagendijk, M. Schlottbom, J. J. W. van der Vegt, and W. L. Vos, Scaling theory of wave confinement in classical and quantum periodic systems, Phys. Rev. Lett. **129**, 176401 (2022).
[24] M. Kozoň, R. Schrijver, M. Schlottbom, J. J. W. van der Vegt, and W. L. Vos, Unsupervised machine learning to classify the confinement of waves in periodic superstructures, Opt. Express **31**, 31177 (2023).
[25] From textbook solid state physics [21], it is known from tight binding that the bandwidth of a defect band in 1D is proportional to the coupling constant. In contrast, the bandwidth in 3D depends on a multitude of coupling rates, see Ref. [22]. Thus, in certain directions the bandwidth vanishes, whereas the coupling rate in the same direction is large, yet counteracted by other couplings.
[26] A. Crespi, R. Osellame, R. Ramponi, M. Bentivegna, F. Flamini, N. Spagnolo, N. Viggianiello, L. Innocenti, P. Mataloni, and F. Sciarrino, Suppression law of quantum states in a 3D photonic fast fourier transform chip, Nat. Commun. **7**, 10469 (2016).
[27] F. Hoch, S. Piacentini, T. Giordani, Z.-N. Tian, M. Iuliano, C. Esposito, A. Camillini, G. Carvacho, F. Ceccarelli, N. Spagnolo, A. Crespi, F. Sciarrino, and R. Osellame, Reconfigurable continuously-coupled 3D photonic circuit for boson sampling experiments, npj Quantum Inf. **8**, 55 (2022).
[28] J. Moughames, X. Porte, M. Thiel, G. Ulliac, L. Larger, M. Jacquot, M. Kadic, and D. Brunner, Three-dimensional waveguide interconnects for scalable integration of photonic neural networks, Optica **7**, 640 (2020).
[29] J. Argüello-Luengo, A. González-Tudela, T. Shi, P. Zoller, and J. I. Cirac, Quantum simulation of two-dimensional quantum chemistry in optical lattices, Phys. Rev. Res. **2**, 042013 (2020).
[30] S. E. Skipetrov and I. M. Sokolov, Absence of Anderson localization of light in a random ensemble of point scatterers, Phys. Rev. Lett. **112**, 023905 (2014).
[31] M. Kozoň, A. Lagendijk, M. Schlottbom, J. J. W. van der Vegt, and W. L. Vos, Symmetries and wave functions of photons confined in three-dimensional photonic band gap superlattices, Phys. Rev. B **109**, 235141 (2024).
[32] E. Yablonovitch, Inhibited spontaneous emission in solid-state physics and electronics, Phys. Rev. Lett. **58**, 2059 (1987).
[33] S. John, Strong localization of photons in certain disordered dielectric superlattices, Phys. Rev. Lett. **58**, 2486 (1987).
[34] J. D. Joannopoulos, S. Johnson, J. N. Winn, and R. D. Meade, *Photonic Crystals: Molding the Flow of Light* (Princeton University, Princeton, NJ, 2008).
[35] M. Bayindir, B. Temelkuran, and E. Ozbay, Tight-binding description of the coupled defect modes in three-dimensional photonic crystals, Phys. Rev. Lett. **84**, 2140 (2000).
[36] K. M. Ho, C. T. Chan, C. M. Soukoulis, R. Biswas, and M. Sigalas, Photonic band gaps in three dimensions: New layer-by-layer periodic structures, Solid State Commun. **89**, 413 (1994).
[37] Animation "3D Photonic Crystal with a Diamond Structure" (2012), www.youtube.com/nanocops.
[38] R. W. Tjerkstra, L. A. Woldering, J. M. van den Broek, F. Roozeboom, I. D. Setija, and W. L. Vos, Method to pattern etch masks in two inclined planes for three-dimensional nano- and microfabrication, J. Vac. Sci. Technol. B **29**, 061604 (2011).
[39] D. A. Grishina, C. A. M. Harteveld, L. A. Woldering, and W. L. Vos, Method for making a single-step etch mask for 3D monolithic nanostructures, Nanotechnology **26**, 505302 (2015).
[40] D. A. Grishina, 3D Silicon Nanophotonics, Ph.D. thesis, University of Twente, 2017.
[41] R. Hillebrand, S. Senz, W. Hergert, and U. Gösele, Macroporous-silicon-based three-dimensional photonic crystal with a large complete band gap, J. Appl. Phys. **94**, 2758 (2003).
[42] M. Maldovan and E. L. Thomas, Diamond-structured photonic crystals, Nat. Mater. **3**, 593 (2004).

[43] L. A. Woldering, A. P. Mosk, R. W. Tjerkstra, and W. L. Vos, The influence of fabrication deviations on the photonic band gap of three-dimensional inverse woodpile nanostructures, J. Appl. Phys. **105**, 093108 (2009).
[44] M. Adhikary, R. Uppu, C. A. M. Harteveld, D. A. Grishina, and W. L. Vos, Experimental probe of a complete 3D photonic band gap, Opt. Express **28**, 2683 (2020).
[45] L. A. Woldering, A. P. Mosk, and W. L. Vos, Design of a three-dimensional photonic band gap cavity in a diamondlike inverse woodpile photonic crystal, Phys. Rev. B **90**, 115140 (2014).
[46] In Fig. 3(a) the incident focus is close to the middle defect pore on the XY surface, and in Fig. 3(b) the incident focus is in between the middle and the rightmost defect pore on the XY surface at $X = 2.5$ μm.
[47] S. R. Huisman, R. V. Nair, L. A. Woldering, M. D. Leistikow, A. P. Mosk, and W. L. Vos, Signature of a three-dimensional photonic band gap observed on silicon inverse woodpile photonic crystals, Phys. Rev. B **83**, 205313 (2011).
[48] E. Lidorikis, M. M. Sigalas, E. N. Economou, and C. M. Soukoulis, Gap deformation and classical wave localization in disordered two-dimensional photonic-band-gap materials, Phys. Rev. B **61**, 13458 (2000).
[49] Z.-Y. Li and Z.-Q. Zhang, Fragility of photonic band gaps in inverse-opal photonic crystals, Phys. Rev. B **62**, 1516 (2000).
[50] A. F. Koenderink, A. Lagendijk, and W. L. Vos, Optical extinction due to intrinsic structural variations of photonic crystals, Phys. Rev. B **72**, 153102 (2005).
[51] This procedure is necessary since the nanopore radii vary across the sample surface and depth. Therefore, at every probed location there is effectively a "local" pore radius. In Ref. [44] it is shown that the lower band edge combined with the known gap map [43] gives a reliable estimate of the local pore radius.
[52] The modulation of the upper edge of the measured gap versus position is clearly seen in Fig. 5, where the gap narrows at every defect pore and widens in between.
[53] The sum of the reflectivity and the lateral scattering are less than 100% since our setup can only access part of the light scattered in the $-X$ direction into air, whereas light scattered in the $(+X, \pm Y)$ directions escapes undetected. Since these scattered contributions propagate in the high-index Si substrate, it is conceivable that their contributions are considerably larger than the detected fraction in air, that may in turn also be attenuated by Fresnel reflectivity at the crystal-air interface.
[54] M. P. van Albada, M. B. van der Mark, and A. Lagendijk, Polarisation effects in weak localisation of light, J. Phys. D **21**, S28 (1988).
[55] P. W. Anderson, Absence of diffusion in certain random lattices, Phys. Rev. **109**, 1492 (1958).
[56] P. R. Villeneuve, S. Fan, and J. D. Joannopoulos, Microcavities in photonic crystals: Mode symmetry, tunability, and coupling efficiency, Phys. Rev. B **54**, 7837 (1996).
[57] S. A. Rinne, F. García-Santamaría, and P. V. Braun, Embedded cavities and waveguides in three-dimensional silicon photonic crystals, Nat. Photon. **2**, 52 (2008).
[58] K. Ishizaki, M. Koumura, K. Suzuki, K. Gondaira, and S. Noda, Realization of three-dimensional guiding of photons in photonic crystals, Nat. Photon. **7**, 133 (2013).
[59] T. Tajiri, S. Takahashi, Y. Ota, K. Watanabe, S. Iwamoto, and Y. Arakawa, Three-dimensional photonic crystal simultaneously integrating a nanocavity laser and waveguides, Optica **6**, 296 (2019).
[60] S. Rotter and S. Gigan, Light fields in complex media: Mesoscopic scattering meets wave control, Rev. Mod. Phys. **89**, 015005 (2017).
[61] R. Uppu, M. Adhikary, C. A. M. Harteveld, and W. L. Vos, Spatially shaping waves to penetrate deep inside a forbidden gap, Phys. Rev. Lett. **126**, 177402 (2021).
[62] R. Uppu, F. T. Pedersen, Y. Wang, C. T. Olesen, C. Papon, X. Zhou, L. Midolo, S. Scholz, A. D. Wieck, A. Ludwig, and P. Lodahl, Scalable integrated single-photon source, Sci. Adv. **6**, eabc8268 (2020).
[63] A. Tandaechanurat, S. Ishida, D. Guimard, M. Nomura, S. Iwamoto, and Y. Arakawa, Lasing oscillation in a three-dimensional photonic crystal nanocavity with a complete band gap, Nat. Photon. **5**, 91 (2011).
[64] J.-M. Lourtioz, H. Benisty, V. Berger, J.-M. Gérard, D. Maystre, and A. Tchelnokov, *Photonic Crystals* (Springer Verlag, Berlin, 2008).
[65] A. F. Koenderink and W. L. Vos, Light exiting from real photonic band gap crystals is diffuse and strongly directional, Phys. Rev. Lett. **91**, 213902 (2003).
[66] J. M. van den Broek, L. A. Woldering, R. W. Tjerkstra, F. B. Segerink, I. D. Setija, and W. L. Vos, Inverse-woodpile photonic band gap crystals with a cubic diamond-like structure made from single-crystalline silicon, Adv. Funct. Mater. **22**, 25 (2012).
[67] M. J. Goodwin, C. A. M. Harteveld, M. J. de Boer, and W. L. Vos, Deep reactive ion etching of cylindrical nanopores in silicon for photonic crystals, Nanotechnology **34**, 225301 (2023).
[68] W. Setyawan and S. Curtarolo, High-throughput electronic band structure calculations: Challenges and tools, Comput. Mater. Sci. **49**, 299 (2010).
[69] S. Johnson and J. Joannopoulos, Block-iterative frequency-domain methods for Maxwell's equations in a planewave basis, Opt. Express **8**, 173 (2001).
[70] D. Sharma, S. B. Hasan, R. Saive, J. J. W. van der Vegt, and W. L. Vos, Enhanced absorption in thin and ultrathin silicon films by 3D photonic band gap back reflectors, Opt. Express **29**, 41023 (2021).
[71] M. S. Thijssen, R. Sprik, J. E. G. J. Wijnhoven, M. Megens, T. Narayanan, A. Lagendijk, and W. L. Vos, Inhibited light propagation and broadband reflection in photonic air-sphere crystals, Phys. Rev. Lett. **83**, 2730 (1999).
[72] G. Ctistis, A. Hartsuiker, E. van der Pol, J. Claudon, W. L. Vos, and J. M. Gérard, Optical characterization and selective addressing of the resonant modes of a micropillar cavity with a white light beam, Phys. Rev. B **82**, 195330 (2010).
[73] Multiple authors, New Semiconductor Materials NSM Archive, Ioffe Institute, St. Petersburg, URL: http://www.ioffe.ru/SVA/NSM/Semicond/.
[74] The Si reflectivity spectrum has a small positive slope with frequency since we do not consider the change of refractive index with frequency within this range.
[75] S. Y. Lin and G. Arjavalingam, Tunneling of electromagnetic waves in two-dimensional photonic crystals, Opt. Lett. **18**, 1666 (1993).
[76] Y. A. Vlasov, V. N. Astratov, O. Z. Karimov, A. A. Kaplyanskii, V. N. Bogomolov, and A. V. Prokofiev, Existence of a photonic

pseudogap for visible light in synthetic opals, Phys. Rev. B **55**, R13357 (1997).

[77] Y. Neve-Oz, M. Golosovsky, D. Davidov, and A. Frenkel, Bragg attenuation length in metallo-dielectric photonic band gap materials, J. Appl. Phys. **95**, 5989 (2004).

[78] A. Yariv and P. Yeh, Electromagnetic propagation in periodic media, in *Optical Waves in Crystals: Propagation and Control of Laser Radiation* (Wiley, New York, 1980).

[79] D. Devashish, S. B. Hasan, J. J. W. van der Vegt, and W. L. Vos, Reflectivity calculated for a three-dimensional silicon photonic band gap crystal with finite support, Phys. Rev. B **95**, 155141 (2017).

[80] J. Goodman, *Speckle Phenomena in Optics: Theory and Applications* (Roberts & Company, Englewood, Colorado, 2007).

[81] J. C. Dainty, *Laser Speckle and Related Phenomena*, Topics in Applied Physics (Springer, Berlin, 2013).